Materials Advances

ROYAL SOCIETY OF CHEMISTRY

PAPER

View Article Online
View Journal

Cite this: DOI: 10.1039/d6ma00227g

Enhanced faradaic pseudo-capacitance in a reduced π-conjugated carbon network anchored with strontium tungstate nano-hybrids for high-energy supercapacitors

Sabarikaruthapandi Ramar, [a] Sathish Kumar Ponnaiah, [b] Bharathi Kannan Raja, [a] Muthukumar Govindaraj [ac] and Arockia Selvi J *[a]

Received 17th February 2026,
Accepted 24th April 2026

DOI: 10.1039/d6ma00227g

rsc.li/materials-advances

The development of high-performance electrode materials is essential for next-generation supercapacitor (SC) technologies. Herein, $SrWO_4$/rGO hybrid nanostructures were synthesized to enhance electrochemical performance through the synergistic effect of conductive $SrWO_4$ and high-surface-area reduced graphene oxide (rGO). The hybrid electrode exhibits excellent electrochemical performance, delivering an excellent specific capacitance of 727 F g^{-1} at 1 A g^{-1} and retaining 95% of its capacitance over 5000 cycles, indicating long-term stability. The assembled symmetric two-electrode cell ($SrWO_4$/rGO@NF//$SrWO_4$/rGO@NF) operates within a 1.6 V potential window in 1 M KOH electrolyte and shows excellent rate capability. Electrochemical impedance spectroscopy of a symmetric cell reveals low charge-transfer resistance and efficient ion diffusion. The Ragone plot indicates an impressive energy density of 26.13 Wh kg^{-1} at a power density of 2159.5 W kg^{-1} for the assembled symmetric cell. This exceptional performance is attributed to the synergistic effects of conductive $SrWO_4$ and the higher surface area of the resorted π-conjugated rGO structure, enabling efficient charge transport and abundant electroactive sites. These results highlight a promising strategy for developing advanced electrode materials for high-performance energy storage systems.

1. Introduction

The urgent need to address fossil fuel scarcity, environmental degradation, and increasing energy consumption has accelerated the development of alternative energy storage and conversion systems. The increasing demand for sustainable and efficient energy storage solutions has spurred extensive research on supercapacitors (SCs), which play an essential role in advancing electronics, electric vehicles, and renewable energy technologies.[1–3] Due to their high-power density, rapid charge/discharge rates, and excellent cycling stability, SCs stand as effective alternatives to conventional batteries.[4–6] To meet growing energy demands, it is essential to develop durable, high-performance systems that integrate technologies.[7–9]

In this context, SCs are broadly classified into three categories: electrochemical double-layer capacitors (EDLCs), which store charge *via* non-faradaic charge separation; pseudocapacitive materials, which rely on fast and reversible redox reactions; and hybrid capacitors, which combine both pseudocapacitive and non-faradaic double-layer (NFDL) charge storage mechanisms. Among these, hybrid capacitors have emerged as a particularly promising approach for enhancing SC performance due to their ability to deliver high energy density, stable operating voltage, high specific capacitance, and excellent cycling stability. Consequently, extensive efforts have been devoted to exploring SC electrodes, including ternary metal oxides (TMOs) and binary metal oxides (BMOs) that contain at least one electrochemically active metal cation and an oxygen anion. Both pure and bimetallic oxide materials can synergistically enhance capacitive performance by offering improved stability, wider potential windows, higher conductivity, greater reversible capacity, and more active sites.[10–18] Among BMOs, inorganic structured metal oxides such as Scheelite-type metal tungstates with the formula MWO_4 (where M = Ni, Mg, Zn, Sr, Cu, Co, Ba, Ca, Mn, *etc.*) are being investigated for various electrochemical applications, including energy storage.[19,21] Among others, strontium tungstate ($SrWO_4$) has gained

[a] *Department of Chemistry, SRM Institute of Science and Technology, Kattankulathur 603203, Tamil Nadu, India. E-mail: arockiaj@srmist.edu.in, sr9651@srmist.edu.in, br4149@srmist.edu.in*
[b] *Department of Chemical Engineering, Pohang University of Science and Technology (POSTECH), Pohang 37673, Republic of Korea. E-mail: skponnaiah@postech.ac.kr*
[c] *Institute of Industrial Science, The University of Tokyo, 4-6-1 Komaba, Meguro-Ku, Tokyo 153–8505, Japan. E-mail: gmkumar2712@gmail.com, gmkumar@iis.u-tokyo.ac.jp*

particular attention, owing to its high conductivity, ordered crystal structure, and abundant oxygen vacancies.[22–24] This performance is attributed to its crystal structure, in which Sr^{2+} occupies octahedral sites, and W^{6+} is coordinated within tetrahedral oxygen frameworks, which promote structural defects and generate numerous active sites.[25,26] Similarly, carbon-based materials such as graphitic carbon nitride (g-C_3N_4), activated carbon, and carbon nanotubes (CNTs) have emerged as promising candidates for various electrochemical applications, including electrochemical sensors and SC electrodes, owing to their large surface areas and excellent electrical conductivity. Despite these advantages, designing novel or modified electrode materials with improved specific capacitance remains a key challenge for researchers. Though $SrWO_4$ is electrochemically active, it has a lower surface area due to its dense scheelite crystal structure. An effective electrocatalyst for SC requires both electrical conductivity and a high surface area to achieve higher capacitance. Hence, in this work, we aim to anchor electrochemically active and conductive $SrWO_4$ with a resorted π-conjugated structure of graphene oxide post reduction to fabricate a $SrWO_4$/rGO hybrid nanostructure that synergistically combines the high electrical conductivity of $SrWO_4$ and redox-active characteristics with the high surface area of rGO.

Reduced graphene oxide (rGO) is widely recognized as an excellent electrode material due to its restored π-conjugated structure, semiconducting nature, sp^2-hybridised carbon network, and residual functional groups with lone-pair electrons, which collectively facilitate effective interactions with various nanomaterials.[27,28] The sp^2-hybridised carbon in rGO links aromatic carbon domains, thereby further enhancing electrochemical performance.[29,30] The rGO sheets tend to restack face-to-face due to strong π–π interactions, which significantly diminishes their electrochemical performance.[31] Therefore, incorporating $SrWO_4$ as a pseudocapacitive component prevents graphene aggregation and improves specific capacitance.[32,33] There were reports that presented $SrWO_4$-based electrode materials for SC applications; for instance, S. Rajkumar *et al.* fabricated a $SrWO_4$/PPy electrode and achieved a high specific capacitance (747 F g^{-1} at 5 mV s^{-1}) with good stability (5000 cycles).[11] In addition, E. Umar *et al.* designed well-established $SrWO_4$/g-C_3N_4, which shows improved electrochemical performance for both the HER and a hybrid energy storage device.[34] Furthermore, B. Muthukutty *et al.* prepared $SrWO_4$ anchored in a boron nitride matrix, which exhibited improved electrochemical performance for electrochemical sensing of ornidazole.[19] These reports demonstrate $SrWO_4$ hybrid structures capable of achieving high electrochemical performance through morphological tuning, interface engineering, surface modifications, and the fabrication of hybrid nanocomposite. In a broader context, metal tungstates (WO_4^{2-}) have attracted significant attention due to their excellent electrochemical, magnetic, and catalytic properties, making them promising candidates for energy storage applications. For example, Naderi *et al.* demonstrated that $CoWO_4$/nitrogen-doped reduced graphene oxide ($CoWO_4$/NRGO) sheets exhibit a high specific capacitance of 597 F g^{-1} at 5 mV s^{-1} in a 2 M H_2SO_4 electrolyte, with only a 2.9% decay after 4000 cycles.[35] Similarly, Sohouli *et al.* synthesized nanosphere-like MnO_2/$CoWO_4$/NCNO *via* a hydrothermal method and reported a specific capacitance of 536 F g^{-1} at 2 A g^{-1} in a 6 M KOH electrolyte, demonstrating excellent suitability for SC applications.[36] Even though metal-tungstate-based electrode materials have advanced, their poor electrical conductivity and limited surface area limit their practical applications. Therefore, to improve the charge transport and electroactive surface sites, we report a facile one-pot strategy for the preparation of a ternary oxide $SrWO_4$/rGO nanocomposite *via* a reaction between $Na_2WO_4{\cdot}2H_2O$, $SrCl_2{\cdot}6H_2O$, and rGO dispersion. Nanocrystalline $SrWO_4$ on rGO was formed *via* a simple, low-temperature hydrothermal process that exploits $SrWO_4$'s electrochemically active sites while suppressing rGO restacking, thereby enhancing electrochemical performance. As expected, the $SrWO_4$/rGO electrode exhibited excellent SC performance, characterized by high specific capacitance, outstanding cycling stability, and remarkable reversibility. These enhanced properties are attributed to the material's improved electrical conductivity, shortened ion diffusion pathways, and the direct integration of the active material onto a conductive substrate.

2. Experimental section

2.1 Synthesis of $SrWO_4$ nanospheres

All reagents and chemicals utilized were of analytical grade and did not require further purification. The hydrothermal method was employed to synthesise strontium tungstate nanospheres, with minor modifications relative to our previous reports.[20] The materials were dissolved and recrystallized in solvents under elevated temperatures and pressures.[37] Specifically, 30 mL of deionized (DI) water was utilized to separately dissolve 1.3 g of $Na_2WO_4{\cdot}2H_2O$ and 1.0 g of $SrCl_2{\cdot}6H_2O$. During ultrasonication, the $SrCl_2{\cdot}6H_2O$ solution was gradually added dropwise into the $Na_2WO_4{\cdot}2H_2O$ mixture. The resulting homogeneous solution was then securely sealed and ultrasonically agitated for 1 h at room temperature. A few drops of HCl or NaOH were added to adjust/maintain the pH. After continuous agitation using a magnetic stirrer, the reaction solution was moved to a stainless-steel autoclave and kept at 120 °C for 12 h. A white precipitate was formed at the end of the process. After centrifugation, the precipitate was carefully washed with ethanol and DI water and dried for 12 h at 80 °C. Lastly, a muffle furnace was used to calcine the $SrWO_4$ powder for 3 h at 300 °C.

2.2 Synthesis of the $SrWO_4$/rGO nanocomposite

Graphene oxide (GO) was synthesized using the controlled Hummers' method.[2] $SrWO_4$/rGO nanocomposite were synthesized *via* a one-pot, hydrothermal process. Initially, 60 mL of DI water was utilized to disperse 0.02 g of GO powder, followed by ultrasonication for 2 h to remove any unexfoliated GO. The obtained exfoliated GO (EGO) was then dried at 45 °C for 24 h. Subsequently, 100 mg of EGO was dispersed in 400 mL of distilled water under continuous stirring and heated at 95 °C for 4 days to obtain a stable, clear, light-brown rGO suspension.

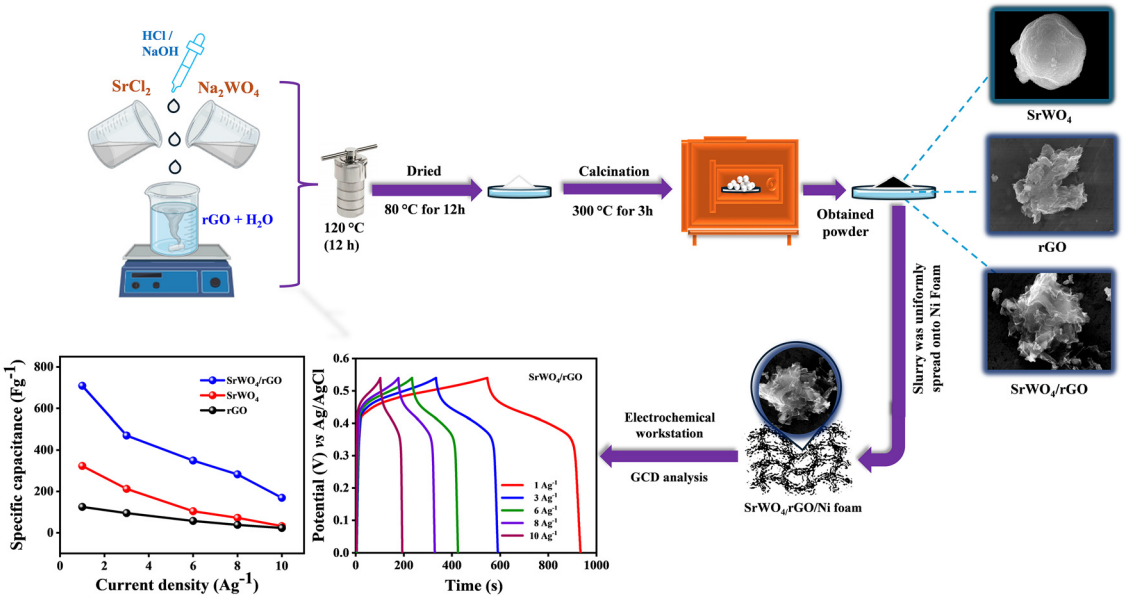

Scheme 1 Schematic illustration of the hydrothermal synthesis of the $SrWO_4$/rGO nanocomposite, and electrochemical analysis with GCD and its specific capacitance curves.

Afterwards, 1.3 g of $Na_2WO_4{\cdot}2H_2O$ and 1.0 g of $SrCl_2{\cdot}6H_2O$ were added to the rGO dispersion and stirred for an additional 2 h. A few drops of HCl or NaOH were added to stabilize pH fluctuations. The resultant mixture was autoclaved at 120 °C for 12 h, and the resulting white precipitate was centrifuged and washed with ethanol and DI water. Finally, the black precipitate was vacuum dried for 8 h at 80 °C. Lastly, a muffle furnace was used to calcine the $SrWO_4$ powder for 3 h at 300 °C, yielding a stable $SrWO_4$/rGO nanocomposite. A schematic illustration of the hydrothermal synthesis of the $SrWO_4$/rGO nanocomposite, and electrochemical analysis with GCD and specific capacitance curves are provided in Scheme 1.

2.3 Electrode fabrication and characterisation

The following procedure was employed to fabricate the modified electrodes and to perform electrochemical analyses at room temperature. The electroactive materials ($SrWO_4$ or rGO or $SrWO_4$/rGO), the binder (polyvinylidene fluoride, PVDF), and the conductive carbon black were mixed in a 8 : 1 : 1 weight ratio. Then, 10 μL of NMP (*N*-methyl-2-pyrrolidone) was added to the powder mixture to form a viscous slurry. The slurry was coated onto a 1 × 1 cm^2 nickel foam (NF) substrate, which served as the working electrode, and dried in a hot air oven at 60 °C.[2] Electrochemical studies were performed using a symmetrical two-electrode SC (STS) with $SrWO_4$/rGO/NF as both electrodes, PVA/KOH gel as the electrolyte, and a microfiber glass filter (0.18 mm thick) as the separator. Electrochemical impedance spectroscopy (EIS), galvanostatic charge–discharge (GCD), and cyclic voltammetry (CV) measurements were performed using a CHI 760E electrochemical workstation in a three-electrode configuration, consisting of platinum wire (counter electrode), saturated Ag/AgCl (reference electrode), and $SrWO_4$, rGO, and $SrWO_4$/rGO (working electrode). The mass of the active material loaded onto the fabricated electrode was 3 mg. The specific capacitance (C_{sp}) was calculated from galvanostatic charge–discharge (GCD) curves using eqn (1).[38,39]

$$C_s = I \times \Delta t/m \times \Delta V \times (\mathrm{F\ g^{-1}}) \quad (1)$$

where m represents the mass of the active material (mg), ΔV denotes the potential window (V), I corresponds to the discharge current (A), and Δt is the discharge time (s).

3. Results and discussion

3.1 Investigation of crystallinity, functional groups, and lattice vibrations of the synthesized materials

The crystallization of $SrWO_4$ and its interaction with rGO occurred simultaneously during the synthesis.[28] X-ray diffraction (XRD) was used to evaluate the phase composition and crystallinity of the synthesized materials. $SrWO_4$ crystallizes in the tetragonal $I4_1/a$ space group and has a structure similar to zircon. Sr^{2+} ions are coordinated by eight equivalent O^{2-} ions, forming an eightfold (eight-coordinate) coordination geometry. W^{6+} ions are coordinated by four equivalent O^{2-} ions, forming a tetrahedral coordination geometry. Each O^{2-} ion is three-fold coordinated, bonding to two equivalent Sr^{2+} ions and one W^{6+} ion, as illustrated in Fig. 1(a). The tetrahedral scheelite-type crystal structure of $SrWO_4$, analogous to that of zircon, underpins its electrochemical performance in a SC by providing a framework of coordinated polyhedra that facilitates redox reactions and ion transport dynamics. (Data retrieved from the materials project for $SrWO_4$ (mp-19163) from database version v2025.09.25.) In addition, the distorted eight-coordinate geometry of Sr^{2+} improves lattice stability and ion diffusion pathways, thereby facilitating electrolyte accessibility and ion diffusion, while the tetrahedral WO_4 units act as

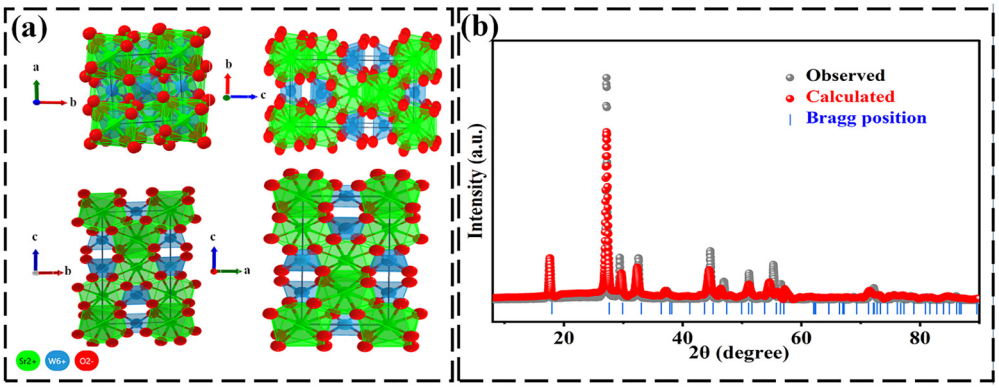

Fig. 1 (a) Crystal structure of $SrWO_4$ in different geometries. (b) Theoretically calculated pattern exhibiting minimal deviation from the Bragg position. Data retrieved from the materials project for $SrWO_4$ (mp-19163) from database version v2025.09.25.

electrochemically active centres that enable faradaic redox reactions involving the W^{6+}/W^{5+} redox couple, contributing to pseudo-capacitance.[11] In this crystal system, each W^{6+} ion is tetrahedrally coordinated by four oxygen ions forming isolated $[WO_4]^{2-}$ units, while Sr^{2+} ions occupy eight-fold coordination; this structural arrangement gives rise to structural disorder and oxygen vacancies, which create localized electronic energy levels and additional active sites. In addition, the presence of W^{6+} and W^{5+} enables reversible faradaic redox transitions, thereby improving the overall electrochemical performance.[40] Pristine $SrWO_4$ typically shows clear and well-defined diffraction peaks matching its tetragonal scheelite structure, indicating a substantially bigger crystallite size and higher crystallinity index, combined with lower micro strain and dislocation density due to its well-ordered lattice (Table S1). This is evidenced by the Rietveld refinement in Fig. 1(b), where the observed XRD pattern and the theoretically calculated pattern exhibit minimal deviation, and both profiles are well aligned with the corresponding Bragg positions. Fig. 2(a) presents the comparative stacked XRD patterns for pure $SrWO_4$, rGO, and the $SrWO_4$/rGO composite. The pattern of pure $SrWO_4$, Fig. 2(a), red curve, shows characteristic peaks for the (112) plane at 27.41° and (004) and (200) planes at 29.8° and 32.9°, displaying sharp and intense peaks, confirming its crystalline nature. These peaks match well with the JCPDS card number 01-089-2568.[32] No secondary peaks were observed, indicating that the

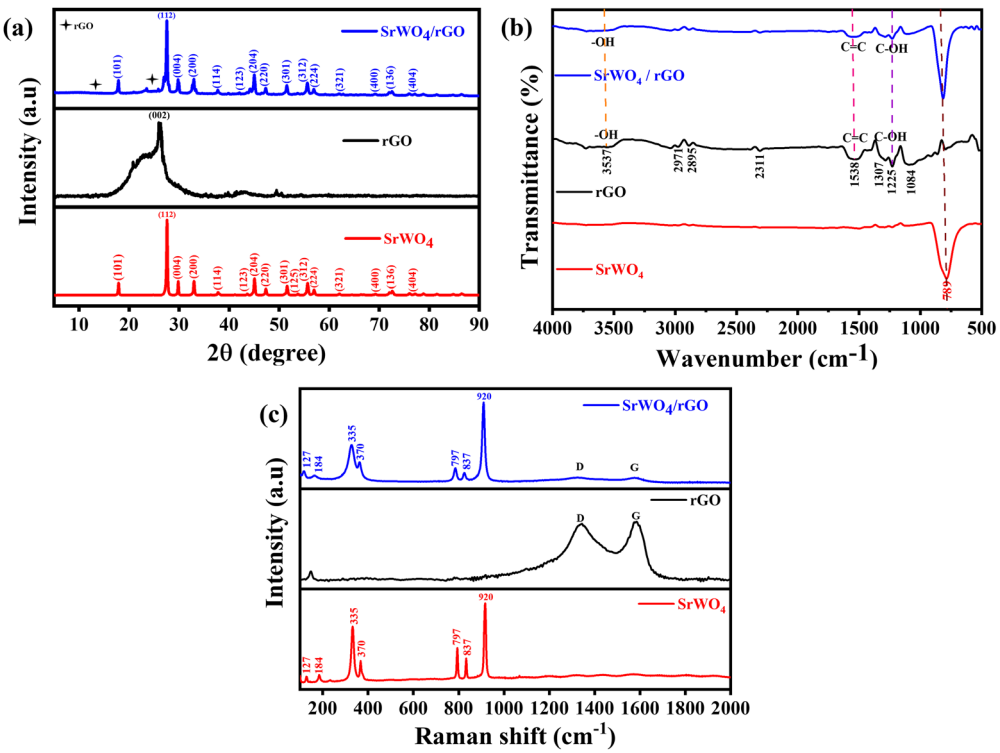

Fig. 2 Crystalline characteristics, phase purity, and material composition: (a)–(c) X-ray diffraction pattern, stacked comparative FT-IR spectrum, and Raman spectra of $SrWO_4$, rGO and the $SrWO_4$/rGO nanocomposite.

synthesized $SrWO_4$ has high phase purity. On the other hand, rGO exhibits a broad, weak diffraction peak, typically around the (002) plane, indicative of higher lattice distortion, smaller effective crystallite domains, poor long-range order, and, consequently, increased microstrain and dislocation density. Strong interfacial interactions between $SrWO_4$ and rGO result in a considerable decrease in crystallite size and crystallinity, as indicated by the XRD peaks of $SrWO_4$/rGO, which remain intact but somewhat widened and decreased in intensity upon composite formation, as shown in Table S1. This interaction introduces additional lattice strain and defects, as evidenced by higher microstrain and dislocation density compared to pure $SrWO_4$. In general, the composite structure strikes a compromise between defect density and crystallinity, which is advantageous for improved electrochemical performance. The XRD analysis of rGO shows two characteristic peaks at 13.18° and 26.68° as shown in Fig. 2(a), black curve, which corresponds to the (100) and (002) crystal planes associated with intra-planar and inter-planar aromatic stacking, respectively, in accordance with JCPDS card number 01-087-1526.[29] Meanwhile, the XRD pattern of the $SrWO_4$/rGO composite (Fig. 2(a), blue curve) reveals no additional or separate crystalline phases. Still, the presence of the rGO (002) peak is clearly evident. Importantly, all characteristic diffraction planes of $SrWO_4$ are also present in the composite, indicating the successful formation of a binary heterojunction structure between $SrWO_4$ and rGO. Furthermore, the crystallite size and microstrain (ε_s) of $SrWO_4$ and $SrWO_4$/rGO were assessed using the Williamson–Hall (W–H) plot. The W–H plots for $SrWO_4$ and $SrWO_4$/rGO are presented as $4\sin\theta$ versus $\beta\cos\theta$ in Fig. S5(c) and (d). The microstrain (ε_s) is obtained from the slope of the linear fit, while the crystallite size is determined from the intercept ($k\lambda/D$, where k = 0.9).[41,42] According to the Scherrer and W–H methods, the average crystallite sizes of $SrWO_4$ and $SrWO_4$/rGO are 30.33 nm and 57.44 nm, respectively. The positive microstrain value ($\varepsilon_s = 2.22 \times 10^{-3}$) indicates the presence of tensile lattice strain. Upon composite formation with rGO, the tetragonal structure of $SrWO_4$ is retained. At the same time, the conductive rGO network provides rapid electron transport pathways to the redox-active $[WO_4]^{2-}$ units, prevents aggregation of $SrWO_4$ particles, and ensures uniform dispersion of the active phase. As a result, the $SrWO_4$/rGO composite achieves a synergistic combination of EDLC from rGO and greatly amplified pseudocapacitance from the tetrahedrally coordinated $SrWO_4$, yielding superior specific capacitance compared to either individual component, while maintaining excellent structural stability and cycling performance owing to the robust tetragonal scheelite framework.

Fourier transform infrared spectroscopy (FT-IR) analysis confirmed the chemical bonds and functional groups present in $SrWO_4$, rGO, and the $SrWO_4$/rGO composite, as evidenced from the stacked comparative FT-IR spectrum, Fig. 2(b). The red curve in Fig. 2(b) represents the spectrum of $SrWO_4$, where bands at 415 and 789 cm^{-1} which are assigned to lattice vibrations associated with the $SrWO_4$ framework.[18] Meanwhile, peaks at 866 and 679 cm^{-1} represent W–O and W–O–W vibrations, whereas the 1124 cm^{-1} band confirms the presence of WO_4^{2-} groups.[22] Thus, the WO_4^{2-} vibrations represent intact tetrahedra, which facilitate W^{6+}/W^{5+} redox-faradaic reactions; this inference aligns with the XRD reports.[34] The black curve in Fig. 2(b) represents rGO's spectrum, which exhibits characteristic absorption bands that appear at 1538 cm^{-1} – corresponding to carbonyl groups of carboxylic derivatives, 1225 cm^{-1} – corresponding to C=C stretching of aromatic rings, and 1084 cm^{-1} – corresponding to the C–OH stretching vibrations. The presence of –OH and C=O in the rGO increases the conductivity and enables rapid ion adsorption.[43] The absorption peaks at 3537 and 1640 cm^{-1} correspond to –OH stretching and H_2O bending vibrations, respectively.[39] The FTIR spectrum of $SrWO_4$/rGO (Fig. 2(b), blue curve) displays the characteristic peaks of both $SrWO_4$ and rGO. The bands near 3395 cm^{-1} (–OH stretching) exhibit a slight negative shift, confirming the effective reduction of rGO in the composite.[44] Overall, these changes in the absorption bands support the fact that $SrWO_4$ is embedded over the rGO sheets, indicating that $SrWO_4$ aligns with the XRD results.

Subsequently, the vibrational features of the materials were analyzed using Raman spectroscopy, as illustrated in the stacked comparative spectrum in Fig. 2(c). The Raman spectrum of $SrWO_4$ displays distinct bands at 327, 365, 794, 827, and 913 cm^{-1}, corresponding to the ν_2(Ag), ν_4(Bg), ν_2(Eg), ν_3(Bg), and ν_1(Ag) vibrational modes, consistent with previous reports.[41] The band at 180 cm^{-1} corresponds to the tetrahedral WO_4^{2-} unit, as shown in Fig. 2(c), red curve.[23] The ν_1(Ag) vibrational mode at 913 cm^{-1} represents tetrahedral rigidity for stable W^{6+}/W^{5+} redox during charge–discharge cycles.[11] In the rGO spectrum (Fig. 2(c), black curve), the characteristic D and G bands appear at 1398 cm^{-1} and 1558 cm^{-1}, corresponding to defect-induced vibrations (sp^3 carbon) and the in-plane E_{2g} mode of sp^2 carbon, respectively. This is consistent with our previous results, where GO exhibited similar D and G bands at ~1336 and ~1595 cm^{-1}.[2] The intensity ratio (I_D/I_G), a key indicator of structural disorder and reduction, increases from 0.83 for GO to 0.897 for rGO, confirming the effective removal of oxygen functional groups and partial restoration of the sp^2 carbon network. This increase is attributed to the formation of smaller yet more numerous graphitic domains, which enhances defect-related scattering. Furthermore, the Raman spectrum of the $SrWO_4$/rGO composite displays all characteristic modes of the individual components, with slight shifts toward lower wavenumbers, indicating strong interfacial interactions. The I_D/I_G ratio in the composite further increases to 0.9–1.02, likely due to bond formation between the rGO sheets and Sr/W ions. Overall, these results confirm the successful synthesis of the $SrWO_4$/rGO composite.[45]

The optical properties of the $SrWO_4$, rGO, and $SrWO_4$/rGO samples were analyzed using UV-visible spectroscopy. As is typical for scheelite-type inorganic phases, the UV absorption spectrum of $SrWO_4$ (Fig. S1, red curve) exhibits a significant absorption peak at 360 nm, attributed to the WO_4^{2-} group.[42] The absorption band centred at 297 nm in rGO, shown in Fig. S1 – black curve, is due to the π–π* transitions of the π

bonds in graphene, indicating the successful reduction of GO to rGO.[27] As shown in Fig. S1 – blue curve, the absorbance intensity of $SrWO_4$/rGO is shifted to a longer wavelength compared to that of rGO. This observed red shift in $SrWO_4$/rGO is attributed to electronic interactions (charge transfer) at the $SrWO_4$-rGO interface.[45]

3.2 XPS, BET surface area, morphology, and particle size analysis

Subsequently, XPS analysis was conducted to examine the atomic and chemical constituents of the materials ($SrWO_4$/rGO). The XPS survey spectrum and the corresponding elemental composition shown in Fig. 3(a), confirms the presence of elements such as Sr, W, C, and O. The core-level spectrum of Sr 3d (Fig. 3(b)) exhibits two distinct peaks at 134.8 and 133.2 eV, for the $3d_{3/2}$ and $3d_{5/2}$ spin–orbit levels.[24] These symmetric doublets confirm the stability of Sr^{2+} in 8-coordinate polyhedra, which facilitates structural stability and electrolyte access.[11] In Fig. 3(c), the W 4f spectrum reveals prominent peaks at 38.41 eV and 35.7 eV for W $4f_{5/2}$ and W $4f_{7/2}$, confirming tungsten in the W^{6+} oxidation state.[46,47] This validates tetrahedral integrity for reversible faradaic redox (W^{6+}/W^{5+}) in charge discharge cycles.[48] The core-level spectrum of O 1s shows two deconvoluted peaks. As illustrated in Fig. 3(d), the peaks located at 530.8 and 532.6 eV correspond to metal–oxygen (M–O) bonds such as W–O and Sr–O, and to chemisorbed oxygen originating from surface hydroxyl groups, respectively.[10] These enhance hydrophilicity, thereby confirming electrolyte wetting.[49] Furthermore, the C 1s spectrum in Fig. 3(e) displays three distinct binding energy peaks at 284.9, 286.3, and 288.6 eV, which are attributed to aromatic carbon species, namely, C–C/C═C, C–O, and O–C═O functional groups, indicating effective GO removal. These results are consistent with previous studies.[50] The XPS measurements confirmed the successful formation of the $SrWO_4$/rGO composite. Due to the synergistic effect of the synthesized $SrWO_4$/rGO, it has potential as an electrochemically active material for SC applications. XRD, Raman spectroscopy, and XPS were used in a mutually confirming framework for the structural analysis of pristine $SrWO_4$, pure rGO, and the $SrWO_4$/rGO composite. The crystalline phase, lattice structure, and crystallite size are the main information revealed by XRD. For instance, the formation of crystalline $SrWO_4$ is confirmed by well-defined diffraction peaks. In contrast, any broadening or decreased intensity indicates decreased crystallinity or structural disorder after cycling. This is further supported by Raman spectroscopy, which examines carbon-related structural features, particularly the D and G bands, which reveal information about defect density and graphitisation; a greater I_D/I_G ratio usually indicates the reduction of GO to rGO and higher defect sites that boost electrochemical activity. On the other hand, XPS confirms the effective formation of the composite by providing surface-sensitive chemical information that identifies elemental composition and oxidation states (*e.g.*, W^{6+}, Sr^{2+}, and C–C/C–O bonding). Together, these findings show that the synergistic combination of crystalline metal oxide frameworks and

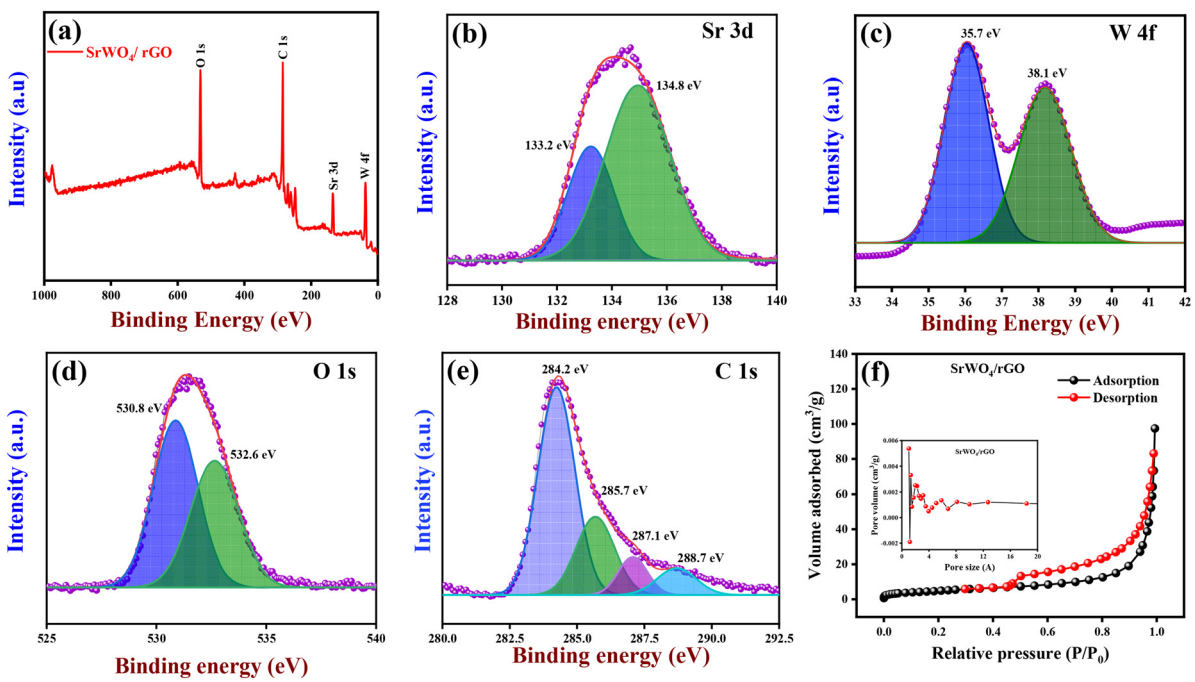

Fig. 3 Material composition, surface chemical statement, and surface area through X-ray photoelectron spectroscopy (XPS) and BET analysis: (a) XPS survey scan of the $SrWO_4$/rGO nanocomposite. Deconvoluted high-resolution XPS spectrum of (b) Sr 3d confirming the $3d_{3/2}$ and $3d_{5/2}$ spin–orbit levels, (c) W 4f confirming tungsten in the W^{6+} with W $4f_{5/2}$ and W $4f_{7/2}$ spin–orbit levels, (d) O 1s confirming metal–oxygen bonds and chemisorbed oxygen originating from surface hydroxyl groups, (e) C 1s confirming the presence of aromatic carbon species and functional groups, indicating effective GO removal and (f) nitrogen adsorption and desorption isotherm of the $SrWO_4$/rGO nanocomposite (inset: pore size distribution curve).

defect-rich conductive carbon networks leads to improved SC performance.[40] Overall, the results from XRD, Raman, and XPS are in good agreement, collectively confirming the structural integrity, vibrational characteristics, and surface chemical composition of the composite, which supports its enhanced electrochemical performance.

The N_2 adsorption–desorption isotherm curves (Fig. 3(f)) were employed to evaluate the specific surface area and pore diameter of the $SrWO_4$/rGO composite. Optimal pore diameter and ideal specific surface area are essential for electrode materials to achieve maximum capacitive performance. The type IV hysteresis loops (Fig. 3(f), inset) reveal numerous mesopores in the hybrid structure, resulting from the integration of rGO nanosheets.[51] The $SrWO_4$/rGO hybrid structure has a specific surface area of 19 m^2 g^{-1}. The BJH (Barrett–Joyner–Halenda) analysis confirms that the $SrWO_4$/rGO hybrid structure is mesoporous, with a pore-size distribution centred at 35.54 Å and a pore volume of 0.1158 cm^3 g^{-1}. Due to their mesoporous structure and accessible surface area, the $SrWO_4$/rGO nanocomposite enhance the electrochemical performance by improving electrode–electrolyte interactions during the reaction.[7]

HR-SEM analysis was used to investigate the structure and surface morphology of $SrWO_4$, rGO, and the $SrWO_4$/rGO composite. HR-SEM images at various magnifications (Fig. 4(a)–(c)) show that bare $SrWO_4$ nanoparticles have a spherical-like structure. The HR-SEM images of rGO at various magnifications (Fig. 4(d)–(f)) reveal scrolled, rippled, and wrinkled features, indicating a large surface area.[52] Fig. 4(g)–(i) illustrate the distorted spherical $SrWO_4$ particles embedded within the rGO composite, highlighting the morphological features of the synthesized $SrWO_4$/rGO composite.

HR-TEM was employed to further investigate the morphological features and size of the synthesized $SrWO_4$, rGO, and $SrWO_4$/rGO nanocomposite (Fig. 5). The HR-TEM images of pure $SrWO_4$ reveal distorted and dispersed spherical nanoparticles (Fig. 5(a) and (b)). The material exhibits a high specific surface area and excellent flexibility, resulting in a crumpled structure. At the same time, interlayer attraction causes a slight stacking of rGO layers. Fig. 5(c) shows that the layered rGO structure typically consists of translucent, sheet-like regions interspersed with wrinkled or folded areas. Electrostatic interactions play a key role in the synthesis process. After adding $SrCl_2$, the negatively charged rGO sheets can adsorb the Sr^{2+} ions. Upon introduction of tungstate salt (Na_2WO_4), WO_4^{2-} anions react with the adsorbed Sr^{2+} to form $SrWO_4$.[20,32] The $SrWO_4$ particles strongly adhere to the rGO sheets, forming a well-integrated $SrWO_4$/rGO composite, as shown in Fig. 5(d)–(f). High-resolution TEM images illustrate the arrangement of atomic planes in $SrWO_4$ (Fig. 5(b)) and rGO (Fig. 5(c)) through the lattice fringes, with their respective interplanar length of 0.457 nm (Fig. 5(g)). Unlike the rest of the sheet, the $SrWO_4$ particles typically appear as black patches. Pure crystallinity of the produced $SrWO_4$/rGO nanocomposite is shown by the bright circular rings seen in the SAED pattern (Fig. 5(h)). Additionally, as shown in Fig. 5(i), the $SrWO_4$/rGO composite contained the expected elements C, O, Sr and W. The EDX spectrum confirmed that the composite was free of contaminants. EDS (EDAX) analysis verifies the elemental composition, showing weight percentages of C (11.0 wt%), O (41.8 wt%), Sr (11.8 wt%), and W (35.4 wt%), demonstrating the presence of all expected elements and confirming the successful formation of the $SrWO_4$/rGO nanocomposite. The corresponding weight percentages of C (32.29 wt%), O (39.62 wt%), Sr

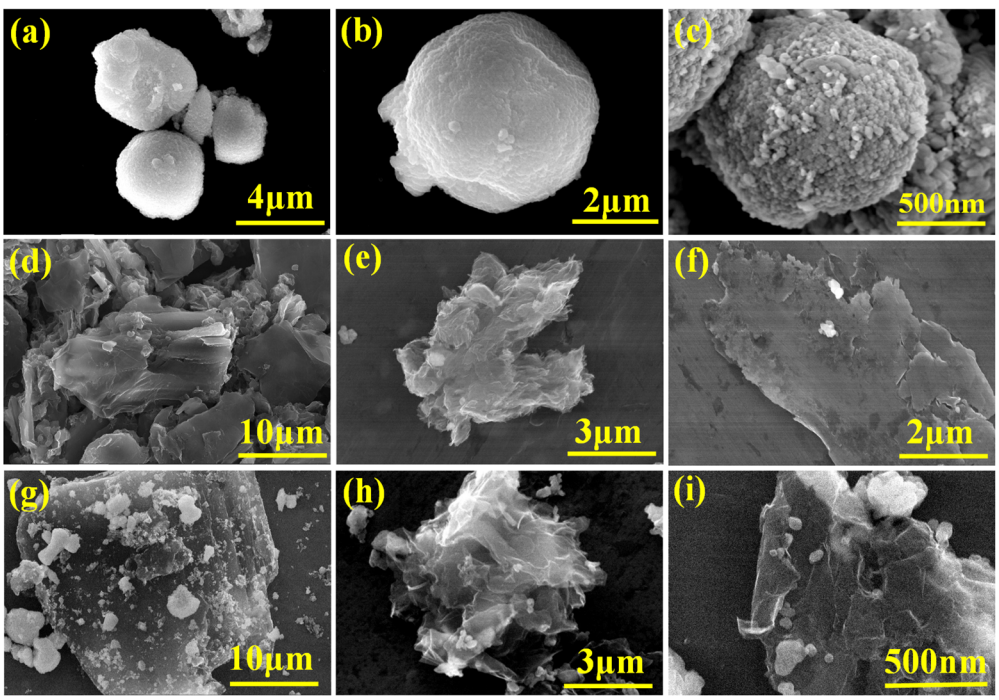

Fig. 4 HR-SEM micrographs of (a)–(c) $SrWO_4$, (d)–(f) rGO, and (g)–(i) the $SrWO_4$/rGO nanocomposite.

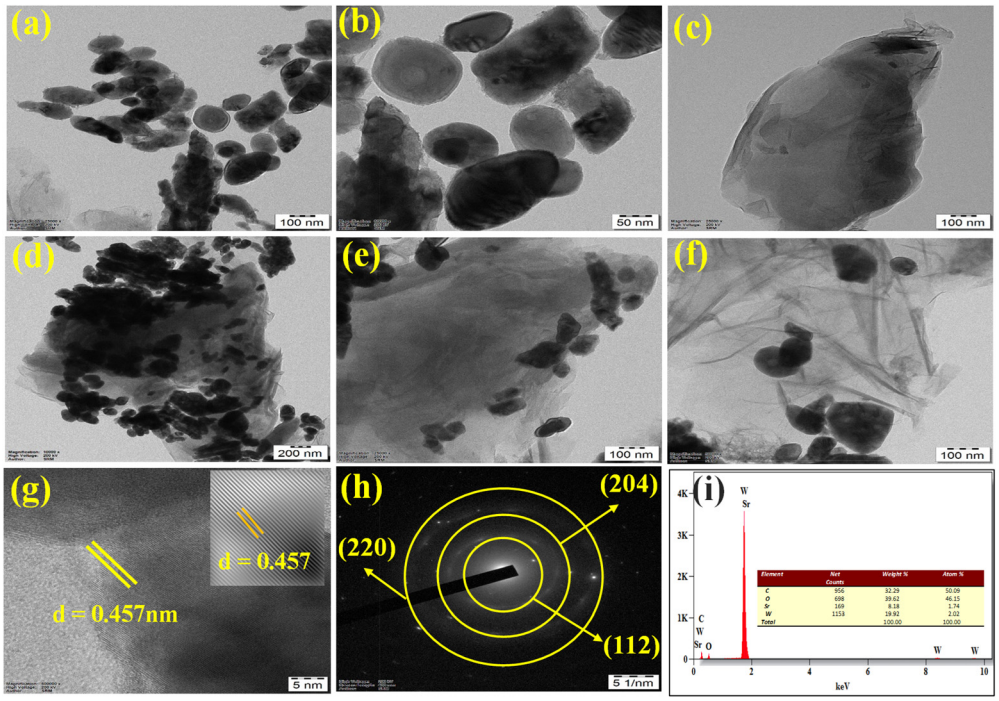

Fig. 5 HR-TEM micrographs of (a) and (b) $SrWO_4$, (c) rGO, and (d)–(f) the $SrWO_4$/rGO nanocomposite, (g) lattice fringes of $SrWO_4$, (h) and (i) SAED pattern and EDX spectrum of the $SrWO_4$/rGO nanocomposite, with the inset (i) table showing the weight and atomic percentages of detected elements.

(8.18 wt%), and W (19.92 wt%) and atomic percentages of C (50.09 wt%), O (46.15 wt%), Sr (1.74 wt%), and W (2.02 wt%) further support the successful formation of the $SrWO_4$/rGO nanocomposite (Fig. 5 (I, inset)).

3.3 Electrochemical performance of the $SrWO_4$/rGO composite

The electrochemical performance of the samples was tested in a 3-electrode system using 1 M KOH as the electrolyte. To evaluate the electrochemical performance, CV and GCD measurements of $SrWO_4$ (red curve) and $SrWO_4$/rGO (blue curve) were carried out at a scan rate of 50 mV s^{-1} and a current density of 1 A g^{-1}, as shown in Fig. S2(a) and (b). CV profiles of $SrWO_4$ exhibited quasi-rectangular curves with broad redox peaks at ~0.4–~0.55 V *vs.* Ag/AgCl, corresponding to the W^{6+}/W^{5+} redox reaction. In contrast, these CV loops expand for $SrWO_4$/rGO with higher capacitance at higher scan rates, indicating rapid ion adsorption on the rGO sheets with a sustained W^{6+}/W^{5+} redox couple.[53,54] These CV and GCD profiles indicate that both $SrWO_4$/rGO exhibit pseudocapacitive behaviour. The smallest integral area in the diagram corresponds to the lowest energy storage capacity. At the same time, the composite's simultaneously highest current magnitude indicates that the $SrWO_4$/rGO hybrid outperforms both $SrWO_4$ and rGO. According to the BET analysis (Fig. 3(f)), the high surface area of $SrWO_4$/rGO improves ion diffusion and likely enhances performance by increasing the number of available ion adsorption sites. The faradaic reactions associated with the pseudo-capacitance effect give rise to redox peaks in the CV and GCD of $SrWO_4$/rGO/NF at 50 mV s^{-1} (Fig. S2(a) and (b), blue curve). In $SrWO_4$/NF, tungsten primarily enhances $SrWO_4$'s conductivity, thereby improving the overall electrochemical capacitance.[55] The CV curves of $SrWO_4$/NF and $SrWO_4$/rGO/NF were tested at scan rates (v) of 10 to 100 mV s^{-1} within 0 to 0.7 V (Fig. 6(a) and (b)). The faradaic mechanism consistently exhibited characteristic pseudocapacitive behaviour, as reflected in the quasi-rectangular shape of the CV curves.[22] Each CV curve shows strong electrochemical reversibility, with nearly symmetrical, well-defined redox peaks, indicating faster redox kinetics for the redox couple (W^{6+}/W^{5+}). Fig. 6(b) shows the CV profile of $SrWO_4$/rGO, where the carbon in the rGO and bimetallic components ($SrWO_4$) contribute to the increased capacitance observed in the composite's integrated area. Peak current rises with scan rate, indicating diffusion-controlled redox at the electrode. An increment in the scan rate shifts the cathodic peaks to lower potential and anodic peaks to higher potentials.[53] The reaction mechanism is associated with the interaction of $SrWO_4$ with hydroxide ions, while the $[WO_4]^{2-}$ groups provide structural stability. The presence of rGO improves the electrical conductivity and facilitates ion transport. When the $SrWO_4$ electrode is immersed in a KOH electrolyte, the following surface reaction occurs, while W does not directly participate in the faradaic reactions:[56–58]

$$SrWO_4 + OH^- \leftrightarrow SrWO_4 - OH + e^- \quad \text{(surface redox reaction)}$$

$$W^{6+} + e^- \leftrightarrow W^{5+} \quad \text{(W redox transition (localized))}$$

The capacitance of $SrWO_4$/NF and $SrWO_4$/rGO/NF materials was evaluated using GCD tests at 1 A g^{-1}, as demonstrated in

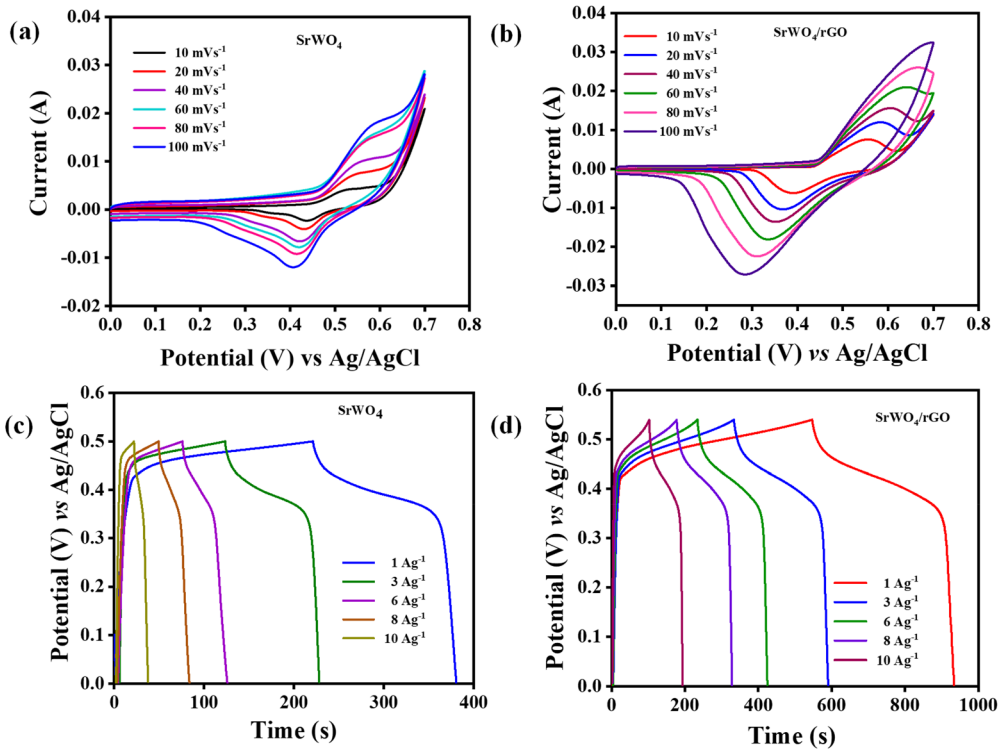

Fig. 6 Electrochemical redox behaviour through CV curves at a scan rate of 10 to 100 mV s^{-1} for (a) $SrWO_4$, and (b) $SrWO_4$/rGO and GCD curves at 1 to 10 A g^{-1} for (c) $SrWO_4$, and (d) $SrWO_4$/rGO in 1 M KOH electrolyte.

Fig. S2(b). Notably, $SrWO_4$/rGO/NF exhibits the most prominent charge/discharge plateau in the GCD curves, which is attributed to its excellent free-electron transport during electrochemical processes, ensuring efficient electron transfer. Likewise, the GCD curves at 1–10 A g^{-1} reveal high electrochemical reversibility and capacitance for both the $SrWO_4$/NF (Fig. 6(c)) and $SrWO_4$/rGO (Fig. 6(d)) SC electrodes. The overall capacitance of $SrWO_4$/NF and $SrWO_4$/rGO/NF comprises surface-controlled capacitance, including reversible double-layer and surface redox pseudo-capacitance, as well as diffusion-controlled capacitance. $SrWO_4$/rGO/NF outperformed several reported materials listed in Table S4. Eqn (2) and (3) are used to further evaluate the nanocomposite's electrochemical performance by applying the power law, relating current density (j) to scan rate (ν):[2,59]

$$j = a\nu^b \quad (2)$$

$$j = k_1\nu = k_2\nu^{\frac{1}{2}} \quad (3)$$

Here, ν and j represent the scan rate and the current density, respectively, while k_1 and k_2 are constants, and both a and b are adjustable parameters.

The slope value (b = 1) denotes a capacitive contribution mechanism, whereas the slope value of (b = 0.5) denotes the diffusion-controlled contribution to charge storage. The capacitive contribution (Dunn method) of $SrWO_4$/NF (Fig. S4(a)–(d)) and $SrWO_4$/rGO/NF (Fig. 7(a)–(d)) decreases at 10 mV s^{-1} and increases to 100 mV s^{-1}. According to Fig. 7(b) and Fig. S4(b), the calculated slope value (b) from the anodic peak currents in 1 M KOH is approximately 0.636 for $SrWO_4$/NF and 0.641 for $SrWO_4$/rGO/NF. This suggests that both diffusion-controlled and capacitive mechanisms drive the reaction.[10] Furthermore, Fig. 7(c) and Fig. S4(c) illustrate the capacitive and diffusive charge contributions of $SrWO_4$/NF and $SrWO_4$/rGO/NF, respectively. The results reveal that the capacitive contribution increases with the scan rate, ranging from 59% to 82% for $SrWO_4$/NF and 86% to 95% for $SrWO_4$/rGO/NF as the scan rate increases from 10 to 100 mV s^{-1}. Moreover, Fig. 7(d) and Fig. S4(d) show plots of the i_p *versus* $\sqrt{\nu}$ for $SrWO_4$/NF and $SrWO_4$/rGO/NF. With anodic and cathodic peak correlation coefficients (R^2) of 0.97 for $SrWO_4$/NF and 0.99 for $SrWO_4$/rGO/NF, the results indicate that the electrode response is predominantly diffusion-controlled.[60] To further understand the charge transfer and ion diffusion behaviour, EIS was performed for the $SrWO_4$, rGO, and $SrWO_4$/rGO electrodes in 1 M KOH over the frequency range of 10 mHz to 100 kHz. As shown in Fig. 8(a)), the Nyquist plots with a high-frequency semicircle and a low-frequency vertical line indicate that the synergistic interaction between $SrWO_4$ and rGO improves both electrical conductivity and charge storage capability.[61] The semicircle diameter represents the interfacial charge transfer resistance (R_{ct}), which is influenced by faradaic processes and double-layer capacitance (C_{dl}). The corresponding data were fitted using a Randles equivalent circuit comprising the solution resistance (R_s), charge-transfer resistance (R_{ct}), double-layer capacitance (C_{dl}), and Warburg impedance (Z_W).[62] The charge transfer kinetics

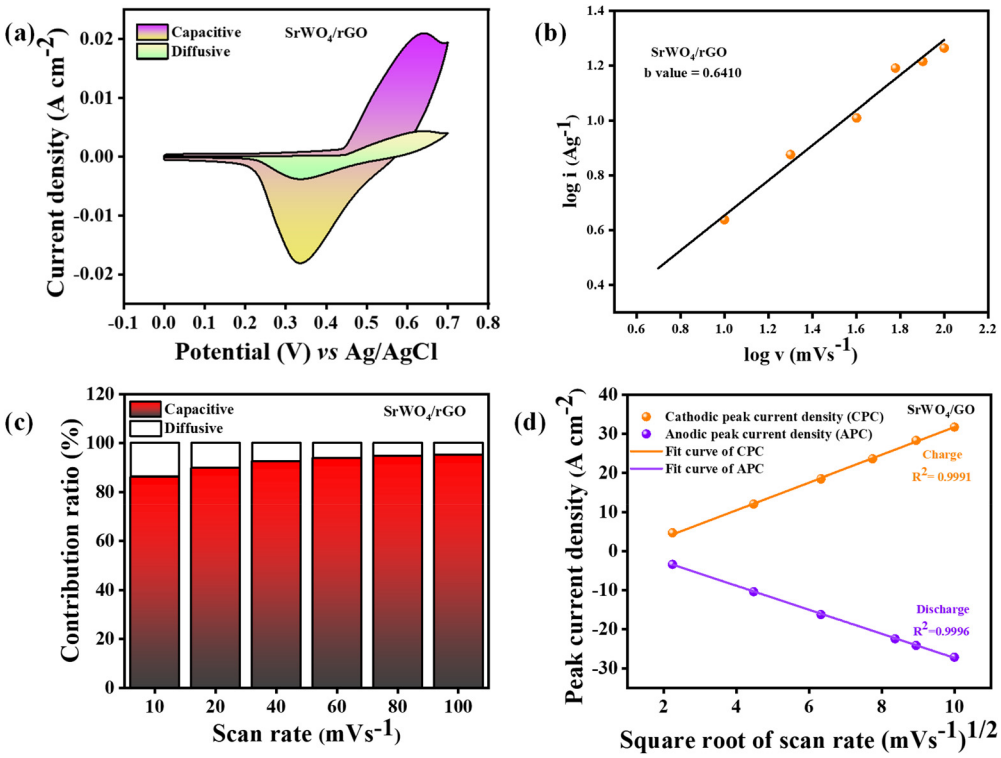

Fig. 7 Dunn method calculation of (a) CV of $SrWO_4$/rGO at 50 mV s^{-1}, (b) logarithmic relationship of scan rate *vs.* peak current density, (c) capacitance contribution of $SrWO_4$/rGO at 10–100 mV s^{-1}, and (d) the square root of the scan rate shown against the peak current density.

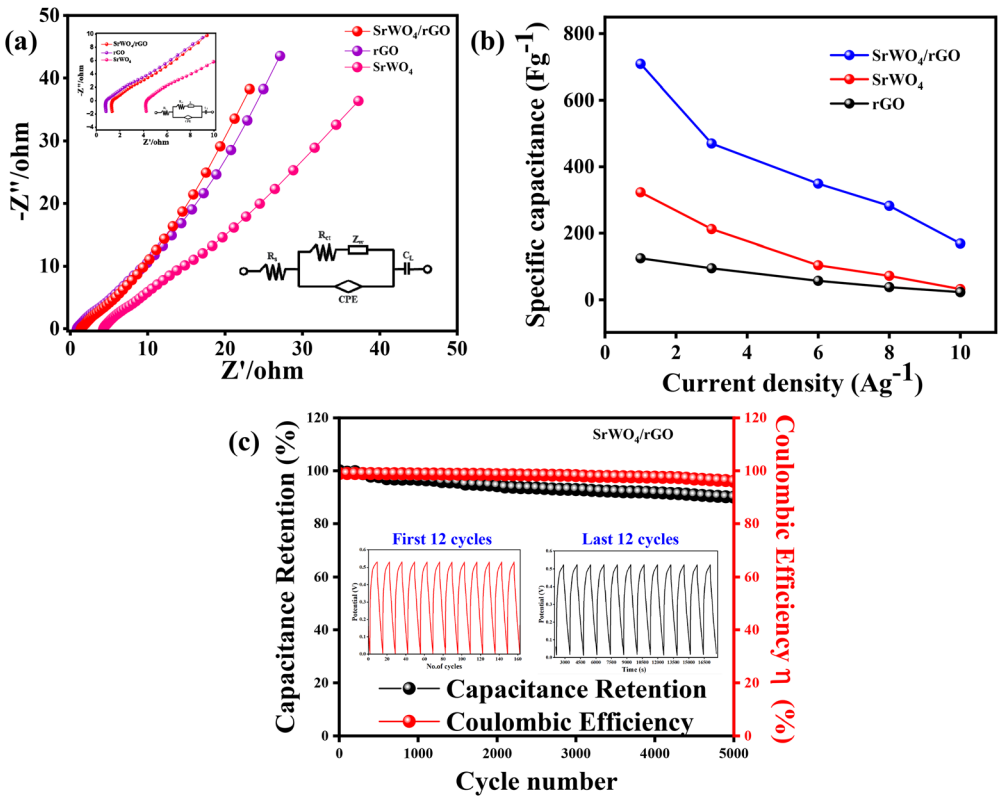

Fig. 8 (a) Interfacial impedance characteristics simulated through Nyquist plots of $SrWO_4$, rGO, and the $SrWO_4$/rGO nanocomposite (inset: zoomed-in image of the high-frequency region). (b) Specific capacitance quantification curves of the various $SrWO_4$ and $SrWO_4$/rGO composite at different current densities 1–10 A g^{-1}, and (c) cycling stability of $SrWO_4$/rGO at 10 A g^{-1} in a three-electrode system (inset: first 12 and last 12 cycles).

and frequency response behaviour of the $SrWO_4$/rGO composite were thoroughly assessed using EIS in both the three-electrode and two-electrode configurations. The Nyquist plot of rGO and $SrWO_4$/rGO in the three-electrode system shows a small compressed semicircle with R_s = 0.8 Ω and R_{ct} = 2.2 Ω, and R_s = 1.3 Ω and R_{ct} = 4.8 Ω, indicating reductions compared to pristine $SrWO_4$ (R_s = 4.2 Ω, R_{ct} = 15.3 Ω) (inset of Fig. 8(a)). The fitted parameters are summarized in Table S2. This confirms that the rGO conductive network significantly reduces both ohmic and kinetic resistances at the material level. In comparison to $SrWO_4$ (τ_0 = 5.88 s) and rGO (τ_0 = 2.22 s), the comparable Bode phase diagram for $SrWO_4$/rGO produces f_0 = 1.16 Hz and τ_0 = 0.86 s, indicating quicker charge–discharge kinetics due to the additional contributions of separator ionic resistance, dual electrode interfaces, and the entire electrolyte bulk path. The EIS parameters in the two-electrode symmetric device configuration show the anticipated increase: R_s = 1.3 Ω and R_{ct} = 4.2 Ω. This is consistent with reports for similar symmetric SC devices, where the two-electrode R_s and R_{ct} values are higher than those for three-electrode devices.[10] Extracted from the two-electrode Bode phase plot, the device-level relaxation time constant (2E) τ_0 = 1.18 s (f_0 = 0.85 Hz) is competitive with similar tungstate-based composite devices, indicating that the practical device maintains the fast kinetic advantages imparted by the rGO scaffold. The superior charge-transport characteristics of the $SrWO_4$/rGO composite for high-performance SC applications are confirmed by a systematic comparison of EIS parameters between the two configurations, which provides a comprehensive kinetic picture that separates the intrinsic material response (three electrodes) from the practical device performance. Notably, the $SrWO_4$/rGO electrode shows the lowest R_{ct}, indicating more efficient electron transport and faster interfacial charge transfer. Fig. S5(c) and (d) present the Bode plots (phase angle and total impedance *versus* frequency). In general, a phase angle approaching 90° at low frequency indicates an ideal capacitive response. Here, the phase angles for $SrWO_4$, rGO, and $SrWO_4$/rGO are around −50°, −54°, and −57° in the low-frequency region, implying a mixed response with a pronounced pseudocapacitive/redox contribution rather than a purely electric double-layer capacitor. Overall, these EIS results support that the redox-active character of the electrode, enhanced by the $SrWO_4$/rGO synergy, is a key factor enabling high total charge storage. Another parameter is the relaxation time constant τ_0, a kinetic parameter obtained from EIS analysis, specifically from the Bode plot (Fig. S6). It clearly explains the minimum time required for a SC electrode to deliver more than 50% of its stored energy with an efficiency greater than 50%.

$$\tau_0 = 1/f_0 \quad (4)$$

where f_0 is the characteristic frequency at which the Bode plot's phase angle equals −45°, or the precise point where the capacitive and resistive impedances match.[63] The τ_0 and f_0 values for $SrWO_4$, rGO and $SrWO_4$/rGO are 5.88 (s), 2.22 (s), 0.86 (s) and 0.17 (Hz), 0.45 (Hz), 1.16 (Hz). The enhanced performance is attributed to the rGO sheets incorporated with $SrWO_4$ particles, which provide a large surface area and porous structure that facilitates rapid electron and ion transport.[32] The $SrWO_4$ and $SrWO_4$/rGO electrode component's faradaic activity is reflected in the GCD curves (Fig. 6(c) and (d)), which exhibit battery-like behaviour at the full current density. At higher charge and discharge rates, this phenomenon is ascribed to restrictions in electrolyte ion mobility.[4] Nonetheless, the $SrWO_4$/rGO electrode (Fig. 8(b)) clearly illustrates the trade-off between specific capacitance of approximately 727, 478, 357, 279 and 168 F g^{-1} at 1, 3, 6, 8, and 10 A g^{-1}, respectively. At higher current densities, limited ion diffusion within the electrode material results in incomplete faradaic reactions at the electrode surface. As a result, when the current density increases, the charge/discharge time decreases. The battery-like features of the GCD curves show the faradaic behaviours of the electrode's ($SrWO_4$/rGO) components over the whole current density range. The C_s values for $SrWO_4$, rGO and $SrWO_4$/rGO at different discharge current densities are shown in Fig. 8(b) in a 1 M KOH electrolyte based on the above-mentioned eqn (4). The cooperative relationship between rGO and $SrWO_4$, which increases the number of active sites for faradaic reactions and improves the charge transfer kinetics, is responsible for this improved performance ($SrWO_4$/rGO). As a result, only a portion of the active surface participates in charge storage, thereby reducing the specific capacitance.[64] When using SC in practical applications, long-term cycling stability is another critical factor to consider. As presented in Fig. 8(c), after 5000 cycles at a current density of 10 A g^{-1}, the $SrWO_4$/rGO electrode retained 95% of its initial capacitance. It also exhibited an outstanding Coulombic efficiency of 96.5%. The first and last twelve cycles from the cycling stability test are shown in the inset of Fig. 8(c). These results indicate that the electrode material maintained excellent stability throughout the cycling process. The first and last ten cycles from the cycling stability test are shown in the inset of Fig. 8(c). Post-cycling XRD (Fig. 10(a) and (b)) and SEM (Fig. 11) analyses both tend to confirm the stability of the material's post-cycles. Pre- and post-cycling stability XRD for $SrWO_4$ and $SrWO_4$/rGO is shown in Fig. S3(a) and (b). The post-cycling XRD pattern has retained all the crystalline peaks of the material compared to the pre-cycling XRD pattern; however, there is a considerable decline in intensity due to lattice distortion caused by expansion/contraction during electrochemical adsorption/desorption. The synthesized $SrWO_4$/rGO electrode exhibits a remarkably high specific capacity in 1 M KOH electrolyte, surpassing that of previously reported metal tungstate-based SC electrodes (Table S3).

3.4 Electrochemical characteristics of the solid-state symmetric supercapacitor

To further evaluate its practical potential, a solid-state symmetrical two-electrode SC (STS) was constructed using $SrWO_4$/rGO as both electrodes (positive and negative). The electrolyte was a 1 M PVA-KOH gel, operating within 0–2.0 V. Fig. 9(a) demonstrates the CV studies of the STS at various scan rates (10–100 mV s^{-1}). Each CV curve exhibits faradaic behaviour and remains consistent across all current densities. Moreover, the current density

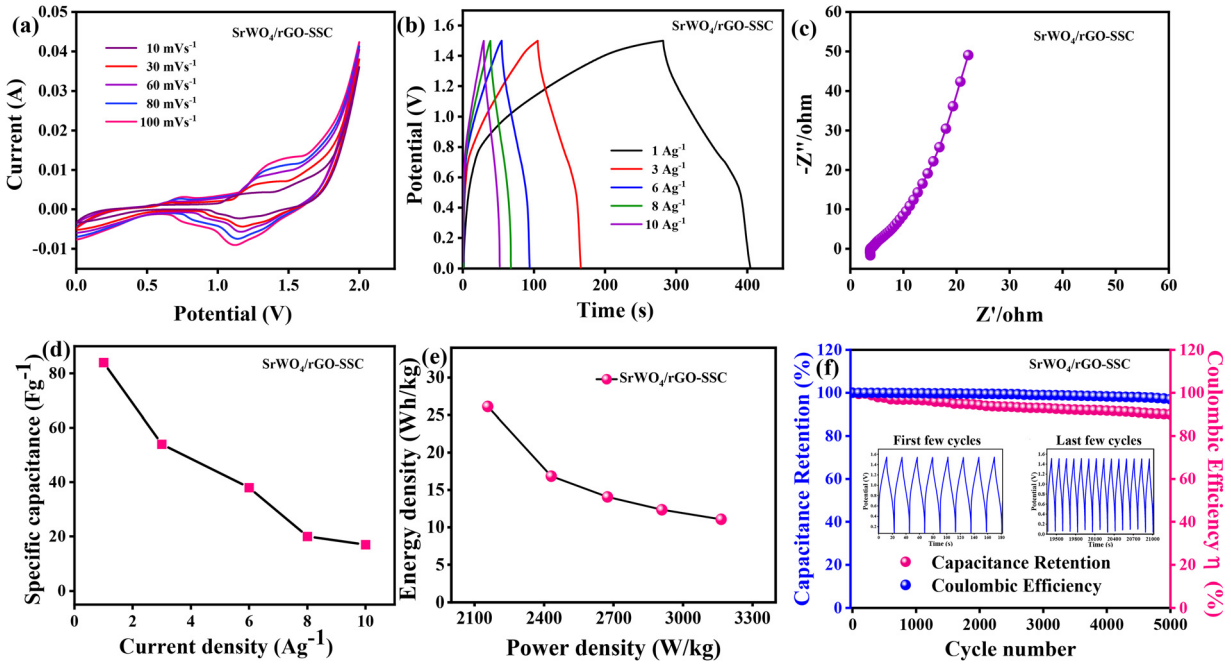

Fig. 9 (a) CV, (b) GCD curves, and (c) EIS spectra for the STS device of $SrWO_4$/rGO//$SrWO_4$/rGO. (d) Specific capacitances of the STS at 1.0 to 10 A g^{-1}. (e) Ragone plot of the STS. (f) Coulombic efficiency and capacitance retention *vs.* the number of cycles for STS (inset: first and last few cycles).

consistently increases with the scan rate, rising from 10 to 100 mV s^{-1}, demonstrating the STS material's excellent rate capability. Likewise, Fig. 9(b) displays the GCD test outcomes within 0–1.5 V at 1 to 10 A g^{-1}. The GCD curves further demonstrate the device's high-power capability by exhibiting characteristic pseudocapacitive behaviour, as evidenced by a nonlinear shape and minimal IR drop across this wide potential range. Fig. 9(c) presents the Nyquist plot of the fabricated device, with the slope indicating the ion adsorption rate within the electrode material. A steeper slope approaching the *y*-axis signifies a higher adsorption rate or improved capacitive performance of the active material. The EIS parameters in the two-electrode symmetric device configuration show the anticipated increase: R_s = 1.3 Ω and R_{ct} = 4.2 Ω. This is consistent with reports for similar symmetric SC devices, where the two-electrode R_s and R_{ct} values are higher than those for three-electrode devices.[10] Extracted from the two-electrode Bode phase plot, the device-level relaxation time constant (2E) τ_0 = 1.18 s (f_0 = 0.85 Hz) is competitive with similar tungstate-based composite devices, indicating that the practical device maintains the fast kinetic advantages imparted by the rGO scaffold. The superior charge-transport characteristics of the STS for high-performance SC applications are confirmed by a systematic comparison of EIS parameters between the two configurations, which provides a comprehensive kinetic picture that separates the intrinsic material response (three electrodes) from the practical device performance. These characteristics indicate that the STS electrode is well-suited for high-performance SC applications. As shown in Fig. 9(d), the following measurements corresponding to Fig. 9(b) were conducted at discharge current densities of 1, 3, 6, 8, and 10 A g^{-1}, and the specific capacitances of the STS were found to be 83.6, 53.9, 38.5, 20.3, and 13 F g^{-1}, respectively. This decrease is attributed to limited ion transport and incomplete utilization of active sites at higher current densities. The energy density (E) and power density (P) of the STS device were calculated using the following eqn (5) and (6):[65]

$$E = \frac{C_s \Delta v^2}{7.2} \left(\text{Wh kg}^{-1}\right) \quad (5)$$

$$P = E/\Delta t \left(\text{W kg}^{-1}\right) \quad (6)$$

where Δt is the discharge time (s), ΔV is the cell operating voltage window, and C_s denotes the specific capacitance (F g^{-1}) of the STS, determined using the total mass of the active materials. Fig. 9(e) presents the Ragone plot of the STS device. The device exhibited a power density of 2159.5 W kg^{-1} at an energy density of 26.13 Wh kg^{-1}, and maintained a stable power density of 3.5 W kg^{-1} with an energy density of 132.8 Wh kg^{-1} at 10 A g^{-1}. For practical STS applications, long-term cycling stability is a key metric. To evaluate the cycling behaviour of the STS electrode, the GCD profiles from the first and last few cycles were compared, as shown in the inset of Fig. 9(f). The STS electrode exhibited remarkable capacity retention of 96.2% and a high Coulombic efficiency of 98.4%, as shown in Fig. 9(f). Despite some performance degradation due to significant volume changes during charge–discharge cycling, which affected the reversibility of the redox reactions, the $SrWO_4$/rGO nanocomposite showed excellent overall stability.[66] To analyze the post-cycling stability of the materials, XRD and SEM were performed. As shown in Fig. 11, the HR-SEM images of the $SrWO_4$/rGO electrode after 5000 cycles reveal

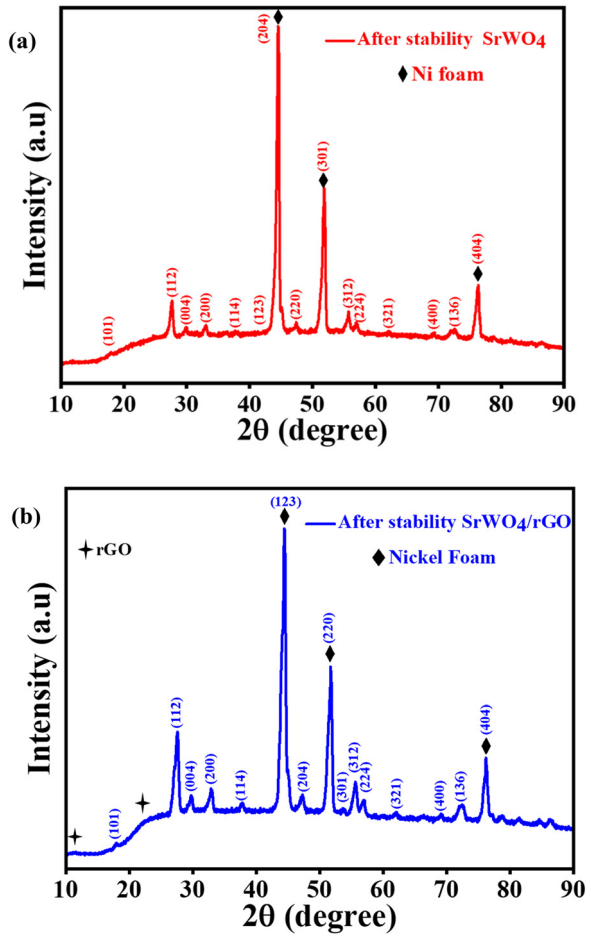

Fig. 10 Post cycling stability XRD for $SrWO_4$ (a) and the $SrWO_4$/rGO nanocomposite (b).

no significant morphological changes, indicating excellent structural stability. The electrode components were recovered *via* ultrasonic dispersion in deionised (DI) water after the stability test. Minor, fragmented, and finer features observed in some regions may result from enhanced adhesion between the active material and the nickel foam (NF), facilitated by the PVDF binder. This improved interfacial adhesion likely contributes to the device's superior long-term cycling stability.[4]

4. Conclusion

In summary, $SrWO_4$/rGO was successfully synthesized *via* a facile one-pot hydrothermal approach, and the resulting nanocomposite was verified using various spectroscopic and analytical techniques. The as-synthesized $SrWO_4$/rGO electrode exhibited superior performance compared to bare $SrWO_4$. At the same time, the porous rGO enhances interfacial contact and increases the number of active sites, thereby augmenting electrolyte interaction. The three-electrode test demonstrated that the $SrWO_4$/rGO electrode achieved an excellent specific capacitance of 727 F g^{-1} at 1 A g^{-1}, and 95% retention after 5000 cycles at 10 A g^{-1}. The high capacitance results from the strategic synergy between rGO's electrical double-layer capacitance and $SrWO_4$'s pseudocapacitive behaviour. Based on this, the synthesized $SrWO_4$/rGO was used as both the positive and negative electrodes to form an STS supercapacitor. The resulting STS device delivered an outstanding specific capacitance of 83.6 F g^{-1}, an energy density of 26.13 Wh kg^{-1} and a power density of 2159.5 W kg^{-1}. The STS system demonstrated exceptional long-term cycling stability, enduring over 5000 cycles, alongside impressive high-rate capability (96.2% reten-

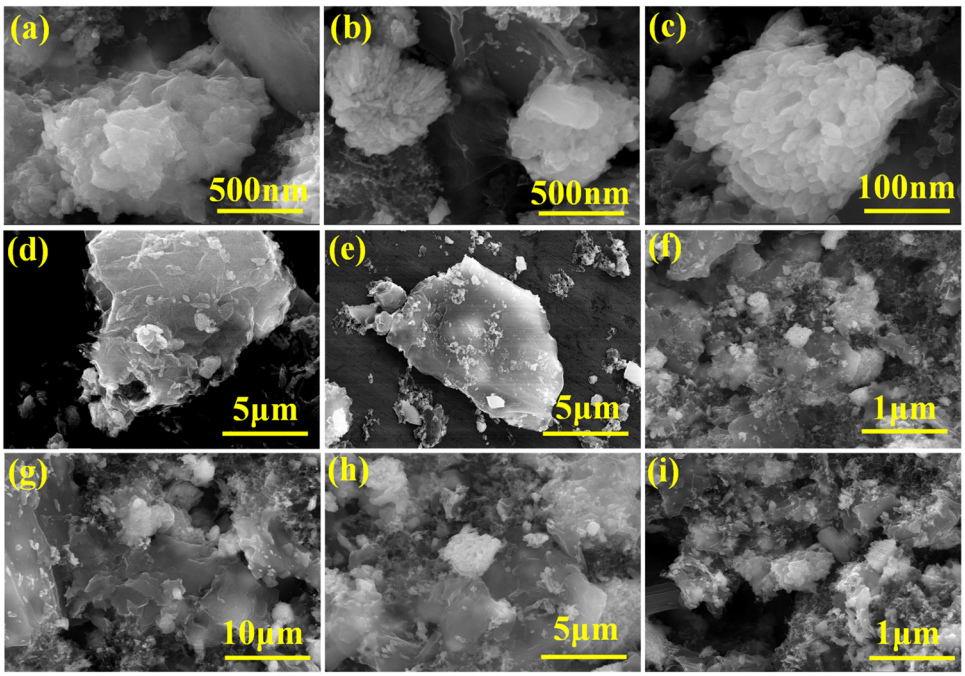

Fig. 11 Post HR-SEM micrographs of (a)–(c) $SrWO_4$, (d) and (e) rGO, and (f)–(i) the $SrWO_4$/rGO nanocomposite.

tion at 10 A g^{-1}). The $SrWO_4$/rGO SC electrode demonstrates significant potential for next-generation energy storage applications, and this study expands the prospects for developing advanced energy storage devices. Future work should systematically examine the effect of $SrWO_4$ on rGO incorporation ratios on the electrochemical behaviour of the hybrid material to further enhance capacitive performance and advance SC applications.

Author contributions

S. R.: conceptualization, formal analysis, experimental operation, validation, data curation, writing original draft, review and editing; P. S.: validation, visualization, data curation, writing review and editing, and revising the manuscript; B. R.: and M. G.: data curation, validation, writing review and editing, and revising the manuscript; J. A. S.: conceptualization, investigation, visualization, supervision, validation, data curation, project administration, resources, and writing review and editing the original manuscript.

Conflicts of interest

The authors declare that they have no known competing financial interests or personal relationships that could have appeared to influence the work reported in this paper.

Data availability

Supplementary information (SI) is available. Associate content: Fig. S1. UV-vis spectra for rGO (black curve), $SrWO_4$ (red curve) and $SrWO_4$/rGO (blue curve). Fig. S2. (a) CV curves at 50 mV S^{-1} and GCD curves at 1 A g^{-1} for $SrWO_4$ (red curve) and $SrWO_4$/rGO (blue curve) in 1 M KOH electrolyte. Fig. S3. (a) CV of $SrWO_4$ at 50 mV S^{-1}, (b) Logarithmic relationship of scan rate *vs* peak current density, (c) Capacitance contribution of $SrWO_4$ at 10–100 mV S^{-1} (d) The square root of the scan rate shown against the peak current density. Fig. S4. (a–b), W–H plot for $SrWO_4$ and $SrWO_4$/rGO, (c–d) Bode phase and Bode plot for $SrWO_4$, rGO, $SrWO_4$/rGO. Fig. S5. (a–b) Bode phase and Bode plot for $SrWO_4$/rGO-SSC. Table S1. Crystalline parameters of the prepared materials. Table S2. Electrochemical impedance parameters. Table S3. Electrochemical performance comparison of metal tungstate-based SCs electrodes. See DOI: https://doi.org/10.1039/d6ma00227g.

Data related to the manuscript content will be made available upon request.

Acknowledgements

We acknowledge the SRM Central Instrumentation Facility (SCIF), the Nanotechnology Research Center (NRC), and the Department of Chemistry for providing research facilities.

References

1 B. Muthukutty, P. Sathish Kumar, D. Lee and S. Lee, *ACS Nano*, 2024, **18**, 27287–27316.
2 S. Ramar, P. Sathish Kumar, M. Govindaraj, M. K. Muthukumaran and B. K. Raja, *Energy Fuels*, 2025, **39**, 10070–10082.
3 M. Karthikeyan, S. Rajkumar and M. Priyadharshan, *J. Ind. Eng. Chem.*, 2025, **147**, 608–618.
4 P. S. Kumar, J. Bae, J. W. Roh, Y. Min and S. Lee, *Nano Convergence*, 2025, **12**, 21.
5 S.-K. Kim, H. J. Kim, J.-C. Lee, P. V. Braun and H. S. Park, *ACS Nano*, 2015, **9**, 8569–8577.
6 S. Rajkumar and J. Qin, in *Supercapacitors: Fundamentals, Advances and Future Applications*, ed. D. K. Verma and J. Aslam, Royal Society of Chemistry, 2025, vol. 3.
7 P. S. Kumar, Y. Min, D. C. Hyun, J.-H. Choi and S. Lee, *J. Energy Storage*, 2023, **74**, 109385.
8 R. P. Dhavale, V. G. Parale, A. M. Teli, N. K. Gupta, U. M. Patil, H. Choi, A. M. Patil, V. D. Phadtare, A. A. Ransing and H.-H. Park, *ACS Appl. Mater. Interfaces*, 2025, **17**, 25193–25205.
9 M. Ganesan, S. Alagar, S. M. Jeong and S. Piraman, *ACS Appl. Nano Mater.*, 2025, **8**, 14531–14546.
10 S. Rajkumar, S. Dhineshkumar, N. Arunprakash, P. Raychel and J. P. Merlin, *Opt. Mater.*, 2023, **142**, 113934.
11 M. D. Angelin, S. Rajkumar, A. Ravichandran, M. M. Alam and A. G. Al-Sehemi, *J. Ind. Eng. Chem.*, 2025, **147**, 436–447.
12 S. Rajkumar and J. Qin, *J. Water Process Eng.*, 2025, **79**, 108920.
13 D. Panda, S. Hota, L. Biswal and R. P. Choudhary, *Trans. Electr. Electron. Mater.*, 2025, **26**, 380–394.
14 S. S. Hota, D. Panda, S. Bhoobash, L. Biswal, S. Mishra and R. N. P. Choudhary, *Polym. Bull.*, 2025, **82**, 7319–7342.
15 S. S. Hota, D. Panda, L. Biswal and R. N. P. Choudhary, *J. Electron. Mater.*, 2024, **53**, 4018–4029.
16 S. S. Hota, D. Panda and R. Choudhary, *J. Korean Ceram. Soc.*, 2024, **61**, 1207–1221.
17 D. Panda, S. S. Hota and R. Choudhary, *J. Solid State Chem.*, 2024, **331**, 124531.
18 D. Panda, S. S. Hota and R. Choudhary, *Inorg. Chem. Commun.*, 2023, **158**, 111501.
19 B. Muthukutty, A. Krishnapandi and S.-M. Chen, *New J. Chem.*, 2020, **44**, 2489–2499.
20 M. Govindaraj, J. Rajendran, U. G. P. K, M. K. Muthukumaran, B. Jayaraman and A. S. J, *ACS Appl. Nano Mater.*, 2023, **6**, 930–945.
21 B. Sriram, M. Govindaraj, S.-F. Wang, S. Kogularasu and A. S. J, *Chem. Eng. J.*, 2025, **519**, 165397.
22 T. Kokulnathan, E. A. Kumar, T.-J. Wang and I.-C. Cheng, *Ecotoxicol. Environ. Saf.*, 2021, **208**, 111516.
23 R. Karthik, P. M. Shafi, S.-M. Chen, R. Sukanya, G. Dhakal and J.-J. Shim, *J. Taiwan Inst. Chem. Eng.*, 2021, **126**, 145–153.
24 D. Sivaganesh, S. Saravanakumar, V. Sivakumar, S. Sasikumar, J. Nandha Gopal, S. Kalpana and

R. Rajajeyaganthan, *J. Mater. Sci.: Mater. Electron.*, 2020, **31**, 8865–8883.
25 J. Rendón-Angeles, Z. Matamoros-Veloza, L. Gonzalez, J. López-Cuevas, T. Ueda, K. Yanagisawa, I. Hernández-Calderón and M. Garcia-Rocha, *Adv. Powder Technol.*, 2017, **28**, 629–640.
26 E. Elanthamilan, S. Rajkumar, S. F. Wang and J. P. Merlin, *Int. J. Energy Res.*, 2022, **46**, 17113–17125.
27 A. Bazan-Aguilar, M. Ponce-Vargas, C. L. Caycho, A. La Rosa-Toro and A. M. Baena-Moncada, *ACS Omega*, 2020, **5**, 32149–32159.
28 S. S. R. Shanlee, M. Govindaraj, T.-W. Chen, S. Ming-Chen, A. S. J, P. C. R. Stella, S. S. Taha, M. F. Elsadek and M. S Elshikh, *Process Saf. Environ. Prot.*, 2026, **210**, 108663.
29 B. Chandran, S. Ramasamy, S. K. Ponnaiah, E. Arumugam, S. Chandrasekaran, S. Karuppaiah and A. Ganesan, *ACS Appl. Nano Mater.*, 2024, **7**, 6839–6850.
30 C. Bhuvaneswari, A. Elangovan, C. Sharmila, K. Sudha and G. Arivazhagan, *Colloids Surf., A*, 2023, **656**, 130299.
31 S. K. Ponnaiah, P. Prakash and B. Vellaichamy, *Ultrason. Sonochem.*, 2018, **44**, 196–203.
32 J. Tang, J. Shen, N. Li and M. Ye, *J. Alloys Compd.*, 2016, **666**, 15–22.
33 S. Sultana, M. A. Parvez, N. R. Singha, M. R. Chandan and M. Rahaman, *ACS Appl. Electron. Mater.*, 2025, **7**, 8732–8799.
34 E. Umar, M. W. Iqbal, F. Shaheen, H. Ullah and R. Wahab, *Electrochim. Acta*, 2025, **510**, 145339.
35 H. R. Naderi, A. Sobhani-Nasab, M. Rahimi-Nasrabadi and M. R. Ganjali, *Appl. Surf. Sci.*, 2017, **423**, 1025–1034.
36 E. Sohouli, K. Adib, B. Maddah and M. Najafi, *Ceram. Int.*, 2022, **48**, 295–303.
37 Y. Zhang, L. Li, H. Su, W. Huang and X. Dong, *J. Mater. Chem. A*, 2015, **3**, 43–59.
38 S. Chinnasamy, J. Madhavan, P. Karthikesan and A. Mani, *J. Power Sources*, 2025, **642**, 236924.
39 N. K. Ravikumar, N. P. S. Chauhan and P. Perumal, *Dalton Trans.*, 2025, **54**, 18046–18063.
40 S. Kaladi Chondath, L. Bansal, B. Sahu and R. Kumar, *ACS Appl. Energy Mater.*, 2025, **8**, 8680–8709.
41 S. S. Hota, D. Panda and R. Choudhary, *Solid State Ionics*, 2023, **399**, 116313.
42 S. S. Hota, D. Panda and R. Choudhary, *Chin. J. Phys.*, 2024, **87**, 430–451.
43 X.-R. Li, Y.-H. Jiang, P.-Z. Wang, Y. Mo, W.-D. Lai, Z.-J. Li, R.-J. Yu, Y.-T. Du, X.-R. Zhang and Y. Chen, *New Carbon Mater.*, 2020, **35**, 232–243.
44 B. RasulKhan, S. K. Ponnaiah, J. Balasubramanian and P. Periakaruppan, *Electrocatalysis*, 2022, **13**, 435–446.
45 X. Liu, Y. Nie, H. Yang, S. Sun, Y. Chen, T. Yang and S. Lin, *Solid State Sci.*, 2016, **55**, 130–137.
46 S. Saravanakumar, D. Sivaganesh, V. Sivakumar, S. Sasikumar, T. Thirumalaisamy, M. Sayed and A. M. Ali, *Phys. Scr.*, 2021, **96**, 125817.
47 M. K. Muthukumaran, M. Govindaraj and A. S. J, *ACS Appl. Nano Mater.*, 2025, **8**, 13381–13393.
48 G. Bakradze, E. Welter and A. Kuzmin, *Materials*, 2024, **17**, 3071.
49 N. Dirany, E. McRae and M. Arab, *CrystEngComm*, 2017, **19**, 5008–5021.
50 X.-M. Yue, Z.-J. Liu, C.-C. Xiao, M. Ye, Z.-P. Ge, C. Peng, Z.-Y. Gu, J.-S. Zhu and S.-Q. Zhang, *Ionics*, 2021, **27**, 339–349.
51 J. Zhang, G. Li, J. Liu, Y. Liu, R. Yang, L. Li, Q. Zhao, J. Gao, G. Zhu and B. Zhu, *Sens. Actuators, B*, 2023, **378**, 133108.
52 D. Manno, L. Torrisi, L. Silipigni, A. Buccolieri, M. Cutroneo, A. Torrisi, L. Calcagnile and A. Serra, *Appl. Surf. Sci.*, 2022, **586**, 152789.
53 S. Ramaraj, M. Sakthivel, S.-M. Chen and K.-C. Ho, *Anal. Chem.*, 2019, **91**, 8358–8365.
54 S. Gadipelli, J. Guo, Z. Li, C. A. Howard, Y. Liang, H. Zhang, P. R. Shearing and D. J. Brett, *Small Methods*, 2023, **7**, 2201557.
55 S. Rajkumar, S. Gowri, S. Dhineshkumar, J. P. Merlin and A. Sathiyan, *New J. Chem.*, 2021, **45**, 20612–20623.
56 U. S. Veerasamy, S. Palani, Y. Fujita, Y. Matsunaga, T. Kuzuya, C. Sekine and Y. Mona, *Adv. Sens. Energy Mater.*, 2025, 100169.
57 R. Iimura, T. Hasegawa and S. Yin, *Inorg. Chem.*, 2022, **61**, 2509–2516.
58 P. Dubey, V. Shrivastav, M. Jain, K. K. Pant, P. H. Maheshwari and S. Sundriyal, *Energy Fuels*, 2023, **37**, 8659–8671.
59 S. M. Abdullah, M. A. Marwat, K. M. Adam, Z. U. Din, M. Humayun, M. R. A. Karim, E. Ghazanfar, M. Bououdina, U. Hamayun and M. S. Youssef, *RSC Adv.*, 2024, **14**, 14438–14451.
60 X. He, Y. Zhao, R. Chen, H. Zhang, J. Liu, Q. Liu, D. Song, R. Li and J. Wang, *ACS Sustainable Chem. Eng.*, 2018, **6**, 14945–14954.
61 S. Gopi and S.-F. Wang, *ACS Appl. Nano Mater.*, 2025, **8**, 924–934.
62 M. Govindaraj, M. K. Muthukumaran, P.-C. Tsai, K. Prakasham, G. Andaluri, M. Eswaran, V. K. Ponnusamy and A. S. J, *Food Chem.*, 2025, **495**, 146387.
63 S. Srivastav, S. Singh and S. K. Meher, *Langmuir*, 2023, **40**, 362–379.
64 E. Elanthamilan, S. Rajkumar, R. Rajavalli and J. P. Merlin, *New J. Chem.*, 2018, **42**, 10300–10308.
65 Z. Yan, S. Luo, Q. Li, Z. S. Wu and S. Liu, *Adv. Sci.*, 2024, **11**, 2302172.
66 F. Zhang, T. Zhang, X. Yang, L. Zhang, K. Leng, Y. Huang and Y. Chen, *Energy Environ. Sci.*, 2013, **6**, 1623–1632.